Journal of Catalysis 450 (2025) 116200

Contents lists available at ScienceDirect

Journal of Catalysis

journal homepage: www.elsevier.com/locate/jcat

Research article

Predicting a generalized mechanism of branched alkane hydrogenolysis on Ru, Ir, and Pt surfaces relevant to polymer upcycling applications

Andy Simonson [a], Lydia Thies [a], David Hibbitts [a,b,*]

[a] Department of Chemical Engineering, University of Florida, Gainesville, FL 32611, USA
[b] Davidson School of Chemical Engineering, Purdue University, West Lafayette, IN 47907, USA

ARTICLE INFO

Keywords:
Hydrogenolysis
Density functional theory
Catalysis
Polymer Upcycling
Depolymerization

ABSTRACT

Here, we present a fundamental study investigating the mechanisms governing C–C hydrogenolysis of branch points within small alkanes on Ir, Pt, and Ru surfaces using Density Functional Theory (DFT). Previous work has shown that activation of unsubstituted C–C bonds occurs through the dehydrogenation of the C–C bond to form a bound alkyne, followed by a kinetically relevant C–C activation and the hydrogenation of the cleaved intermediates to form smaller alkane products. Substituted bonds, in contrast, involve the dehydrogenation of the C–C bond being cleaved, as well as other C atoms near the reacting center. This leads to the counterintuitive observation, that reactions of unsubstituted C–C bonds (having more H to lose) are less inhibited by H_2 than reactions of substituted C–C bonds (having less H atoms to lose). These prior studies of branched alkane activation, however, focused on Ir catalysts and on methyl-substituted alkanes and cycloalkanes, such that the impact of catalyst identity or of long branches (i.e., like those found in some polymers) on substituted C–C hydrogenolysis mechanisms is largely unexplored. Here, we consider isobutane activation mechanisms on Ir, Ru, and Pt catalysts, and use these results to predict how a larger branched alkane, 3-ethylpentane, would react, as that molecule is more reminiscent of the branches in polyethylene. DFT-estimated free energy barriers and turnover rates indicate that hydrogenolysis activity and rate inhibition from hydrogen pressure follow a general trend with catalysts following a reactivity trend of Ru > Ir > Pt, where Ru is the most active and most inhibited by H_2, with Pt being the least reactive and least inhibited by H_2 pressure. By categorizing the isobutane-derived transition states based on whether they are 'extendable' to larger compounds, we predict how the size of branches and the alkane backbone influence substituted C–C bond activation (e.g., comparing isobutane to 3-methylpentane or 3-ethylpentane). These data demonstrate why, on Ru, isobutane hydrogenolysis measurements are unlikely to be informative about the mechanisms that activate branches present in polyethylene or polypropylene molecules. This study lays a foundation for a better mechanistic understanding of how branch points activate in alkanes and relates those changes to polymer upcycling via hydrogenolysis.

1. Introduction

Hydrogenolysis chemistry is significant in many traditional and emerging applications of catalysis including producing undesired light hydrocarbons as a side reaction in refinery streams, [1-3] removing sulfur from process streams, [4,5] upgrading biomass, [6,7] and upcycling inert polymers, such as polyolefins, to generate value from plastic waste [8-10]. Many common plastics are alkanes lacking heteroatoms, such as polyethylene (PE) and Polypropylene (PP), with high resistance to chemical decomposition due to the homogeneity of their structures [11-15]. Metal-catalyzed hydrogenolysis reactions can be used to break C–C bonds within these resistant polyolefins, similar to the use of hydrogenolysis for ring-opening and chain-shortening chemistries of cycloalkanes and alkanes [16-28].

Experimental PE and PP upcycling studies have shown that C–C hydrogenolysis reactions can convert PE and PP into products such as alkanes and aromatic species, using transition metal catalysts, most commonly Ru-based catalysts [8-10,29-51,53]. Ir-based catalysts have been extensively studied for alkane hydrogenolysis in gas phase reactions because it is an undesired side reaction in certain applications [2,3,21,54-58]. For preferential C–C hydrogenolysis, Ru-based catalysts are preferred due to significantly higher rates of C–C cleavage, and have

* Corresponding author at: Davidson School of Chemical Engineering, Purdue University, West Lafayette, IN 47907, USA.
E-mail address: hibbitts@purdue.edu (D. Hibbitts).

https://doi.org/10.1016/j.jcat.2025.116200
Received 3 December 2024; Received in revised form 30 April 2025; Accepted 2 May 2025
Available online 8 May 2025

been demonstrated for upcycling both PE and PP [10,29,32,34,36,39,44]. Pt-based catalysts have successfully decomposed plastic wastes, including upcycling PE and PP to liquid and wax products, [8,38,50,59] upcycling PE into alkylaromatics through a combination of hydrogenolysis and dehydroaromatization, [30] and upcycling aromatic plastic feedstocks into fuels, aromatics, and naphthenes [60-63]. In addition to catalyst choice, hydrogen pressure is a key parameter for controlling the selectivity of hydrogenolysis reactions, as it has been shown to impact the chain length and branching of product distributions from polyolefin hydrogenolysis, [32,44,45,50,52] and this role of H_2 has been partially understood based from model compound studies of branched and linear alkanes [29,64-67].

Previous work has investigated gas-phase C–C hydrogenolysis of C_2–C_{10} linear alkanes, isoalkanes, and cycloalkanes on metal catalysts under high H_2 pressures via both experimental and computational approaches [1-3,21,55-58]. These investigations determined that the general mechanism of C–C bond hydrogenolysis involves a series of mechanistic steps comparable among n-alkanes, [2,3,23,26,27,56,68,69] branched alkanes, [1,28,58] and cycloalkanes [16,21,58,70]. The dissociative adsorption of H_2, hydrocarbon adsorption, and hydrocarbon dehydrogenation elementary steps have been shown to be quasi-equilibrated, forming a pool of partially dehydrogenated intermediates on the catalyst surface (Scheme 1) that are in equilibrium with the gas alkane and H_2 [3,21,68]. This pool of adsorbed hydrocarbons undergo, at varying rates, C–C bond cleavage reactions, the rate-limiting step for alkane hydrogenolysis [3,70]. After the initial C–C bond activation, hydrogenation to produce alkanes is thought to occur rapidly, at least at high H_2/alkane ratios, in kinetically irrelevant steps. While many partially dehydrogenated hydrocarbons are present in this collection of intermediates on the catalyst surface, prior studies indicate that reactions occur through the activation of a small subset of species [1-3,21,57,59]. This general mechanism is shown for the C–C hydrogenolysis of isobutane to form C_1 and C_3 products in Scheme 1.

At high H_2:alkane ratios (typical for gas phase C–C hydrogenolysis), surfaces are predominantly covered by H*, requiring the evolution of H_2 gas to accommodate the adsorption of the alkane, and ultimately to make room for the critical C–C bond activation transition state [3,56,70]. Under these conditions, the mechanism described in Scheme 1 leads to the rate equation:

$$\frac{r}{[L]} = k_{eff}\frac{(C_4H_{10})}{(H_2)^{\lambda}} \tag{2}$$

where (C_4H_{10}) and (H_2) represent gas-phase partial pressures (normalized by 1 bar), and λ reflects the degree of H_2 inhibition, which has been measured for many C–C hydrogenolysis reactions [1-3,21,59]. At steady-state, λ reflects the removal of H atoms from the alkane reactant and the removal of H atoms from a H*-covered surface, both of which result in the formation of H_2 gas through quasi-equilibrated recombinative H_2 desorption [3,56,57,70]. Thus, the measured H_2 pressure dependence (λ) reflects the sum of H* atoms that must desorb from the H*-covered surface (ℓ, the number of sites required) and the number of H atoms removed from the reactant prior to C–C cleavage (y, the extent of dehydrogenation): [1,3,21,57,58]

$$\lambda = \frac{\ell + y}{2} \tag{3}$$

Aside from the general mechanism for C–C hydrogenolysis, prior investigations have also determined several important trends in alkane hydrogenolysis. Notably, the mechanism for activation of unsubstituted C–C bonds among secondary (^{2}C) or primary (^{1}C) atoms in linear alkanes remains consistent regardless of chain length or cleavage position along the chain (and is mostly unaffected by temperature or H_2 pressure at high H_2/alkane ratios). Unsubstituted C–C hydrogenolysis in alkanes and cycloalkanes occurs through the dehydrogenation of the alkane to form a RC*C*R' intermediate, where the R groups can be H atoms (e.g., HC*C*H in ethane hydrogenolysis) or alkyl groups, followed by C–C activation [2,3,56]. The removal of four H atoms from the alkane (y) and two H atoms from the H*-covered surface (ℓ) results in a λ value of 3, consistent with measurements for unsubstituted bond activations in many alkanes and on many metal surfaces at high H_2/alkane ratios [17,21,67,71].

However, for C–C cleavages involving substituted tertiary (^{3}C) or quaternary (^{4}C) carbon atoms, the mechanism differs from the established RC*C*R' intermediate pathway [1,58]. This can be readily rationalized as the tertiary C atoms, for example, can only lose one hydrogen, instead of the two required by the RC*C*R' pathway. Instead, branched C–C bonds activate through pathways where additional C atoms (those not involved in the C–C bond being cleaved) are also dehydrogenated. This leads to a counterintuitive result, that cleaving substituted C–C bonds (which have less hydrogen) occurs after greater dehydrogenation than cleaving bonds with more hydrogen (unsubstituted ones). Instead of a single reaction mechanism, the activation of branched bonds seems to occur through multiple competitive pathways (by prior DFT studies) and is sensitive to the larger structure of the compound, such that isobutane, neopentane, and 2,3-dimethylbutane are predicted to react via distinct mechanisms despite all involving activation at methyl-substituted C atoms.

The H_2-formation reactions are endothermic, replacing C–H and H–M bonds with C–M and H–H bonds, but the evolution of H_2 gas creates entropy, such that increasing temperature can result in the C–C cleavage of more-dehydrogenated species via reactions that have greater activation enthalpies and entropies than cleavage in less-dehydrogenated counterparts [56]. Increasing H_2 pressure has the opposite effect, by reducing the entropic benefits of H_2 gas evolution, it shifts selectivity toward reactions that are less inhibited by H_2 pressure [56,58]. In addition to these shifts in selectivity and reaction mechanism with changing conditions, substituted C–C bond activations have also been shown to react with larger activation enthalpies and H_2-pressure inhibition over unsubstituted bonds [1,16,58,72].

For example, C–C hydrogenolysis at branches within 2-methylpentane and methylcyclohexane exhibit higher degrees of H_2 inhibition compared to hydrogenolysis away from their tertiary C atoms [1,21,58]. Increasing H_2 pressure disproportionately decreases rates C–C cleavage at those branch points, leading to more branched products, and this might also give insights into PE and PP upcycling selectivity trends, given the presence of branched C atoms within those polymers. However prior studies of model branched alkanes focused on methyl-substituted alkanes (e.g., isobutane, 2,3-dimethylbutane, 2-methylpentane, and methylcyclohexane) [1,16,21,58]. Methyl-substituted alkanes may give insights into short branches in PP, but the branches in PE are likely to have longer chains present. Previous work has shown that C–C activations in isobutane and 2,3-dimethylbutane occur with low free energy barriers when one or more of the nearby methyl groups are fully

$$H_2(g) + 2* \rightleftharpoons 2H^* \tag{1.1}$$

$$C_4H_{10}(g) + * \rightleftharpoons C_4H_{10}^* \tag{1.2}$$

$$C_4H_{10}^* + (\ell - 1)^* \rightleftharpoons C_4H_{10-y}^{\ell *} + 0.5y\,H_2(g) \tag{1.3}$$

$$C_4H_{10-y}^{\ell *} \rightarrow C_3H_a^{c*} + CH_b^{d*} \tag{1.4}$$

Scheme 1. General Mechanism for Butane Hydrogenolysis on Metal Catalysts.

dehydrogenated [1]. Such mechanisms, requiring a vicinal methyl group, will not be possible if the nearby chains are longer alkyls.

To understand the role of substituent chain length on the mechanism of activation at branching points in alkanes, we use mechanisms of isobutane to inform the hydrogenolysis of 3-ethylpentane and larger branched alkanes (Fig. 1). Here, we investigate branched C–C cleavage mechanisms for isobutane on Ir(111), Pt(111), and Ru(0001) surfaces using Density Functional Theory (DFT) to determine dominant mechanisms for branched bond activations on each metal. We compare how the reaction rate and mechanism of branched activation are thought to change as you go from more-noble (Pt) to less-noble (Ru) metals. While the hydrogenolysis trends between metals are expected to be the same when considering entire metal nanoparticles with undercoordinated atoms and defects, these results do not include considerations of particle sizes or undercoordinated atoms which would both impact hydrogenolysis rates. We then use these model compound activations to infer the behavior of larger compounds (i.e., to determine whether isobutane activations can be used to predict those in 3-ethylpentane) to describe how effectively one may learn about large compound activations (e.g., in PE macromolecules) from model compound studies.

2. Computational methods

The Vienna *ab initio* Simulation Package (VASP) was used to perform periodic planewave Density Functional Theory (DFT) calculations [73–76] in the computational catalysis interface (CCI) [77]. Planewaves were constructed using projector augmented-wave potentials (PAW) with an energy cutoff of 396 eV [78,79]. The revised Perdew-Burke-Ernzerhof (RPBE) form of the generalized gradient approximation was used to describe exchange and correlation energies [80-82]. Select calculations used the DFT-D3 method [83] to calculate dispersive interaction energies that are absent from the RPBE functional, further discussed below.

Gas-phase molecules were modeled in a $15 \times 15 \times 15$ Å unit cell, and the Brillouin zone of these calculations was sampled at the Γ-point. Ir (111), Pt(111), and Ru(0001) surfaces were modeled as 4×4 periodic lattices, consisting of 4 layers in the z-direction with 10 Å of vacuum space separating slabs. The bottom two layers of the metal surfaces were fixed in their bulk positions, and the top two layers were allowed to relax. Gas-phase and surface structures were optimized using a three-step process involving two geometric convergence steps followed by a single-point calculation to determine electronic energy minima. This three-step convergence process is available in CCI, improving CPU efficiency compared to traditional single-step calculations [77]. Forces on all atoms were calculated using a fast Fourier transform (FFT) grid with a maximum force tolerance of 0.05 eV $Å^{-1}$. In the first and third steps, wavefunctions were converged to within 10^{-4} eV using an FFT grid 1.5x the plane wave cutoff. For the second step, wavefunctions were converged to within 10^{-6} eV using an FFT grid 2x the plane wave cutoff. Optimizations of bare catalyst models used a 4 x 4 x 1 Monkhorst-pack sampling of the first Brillouin zone (k-point mesh) [84,85] for the first two steps and an 8 x 8 x 1 k-point mesh in the third step.

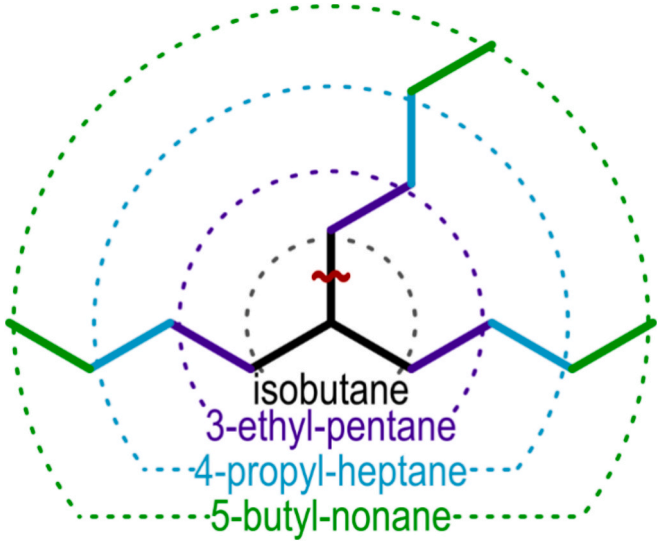

Fig. 1. Model compounds formed from extension of isobutane resembling branch points in PE.

For each elementary reaction, transition state structures were obtained using the nudged elastic band (NEB) [86,87] and dimer [88] methods. The NEB calculations used 16 images, loosely converged to a force below 0.3 eV $Å^{-1}$. Wavefunctions were converged to within 10^{-4} eV using a 3 x 3 x 1 k-point mesh and an FFT grid 1.5x the plane wave cutoff. These NEB calculations provided an estimate of the reaction path and a starting point for the mode and structure of each transition state. The dimer method was then used to optimize transition state structures using a three-step process similar to the three-step method described previously; however, the first two geometric convergence steps used a 3 x 3 x 1 k-point mesh, and the last step used a 6 x 6 x 1 k-point mesh. Reactant and product calculations also used the same optimization process. Analogous VASP settings have been used to study hydrogenolysis and related chemistries in previous work [2,3,55,57,58,89].

Vibrational frequency calculations were performed on all gas-phase molecules and optimized adsorbed species to determine zero-point vibrational energies (ZPVE), vibrational enthalpies (H_{vib}), and vibrational free energies (G_{vib}). Frequency calculations used the fixed displacement method, and all metal atoms were frozen in all frequency calculations, thus avoiding the calculation of M−M vibrational frequencies. These values were used with electronic energies (E_0), obtained from VASP calculations, to estimate enthalpies:

$$H = E_0 + ZPVE + H_{vib} + H_{trans} + H_{rot} \tag{4}$$

and free energies

$$G = E_0 + ZPVE + G_{vib} + G_{trans} + G_{rot} \tag{5}$$

for products, reactants, and transition states.

2.1. Isobutane hydrogenolysis mechanisms

Rates for the rate-determining C–C activation step (Step 1.4 in Scheme 1) of isobutane hydrogenolysis were calculated with the assumption that C–H activation steps within C–C hydrogenolysis mechanisms are quasi-equilibrated, forming a pool of species with variable levels of saturation [3,55,56]. Therefore, rates depend upon the concentration of dehydrogenated hydrocarbon adsorbates that undergo irreversible C–C scission described as:

$$\frac{r}{[L]} = k_{CC}\left[C_4H_{10-y}^{\ell^*}\right] \tag{6}$$

where k_{CC} is the rate constant associated with the C–C bond scission of a particular intermediate that lost y hydrogen atoms in previous C–H activation elementary steps. As previously mentioned, ℓ represents the number of sites required for the transition state to form, and in the case of a covered surface, the number of desorptions of the Most Abundant Surface Intermediate (MASI). Transition state theory and quasi-equilibrium assumptions can be used to describe the formation of the transition state intermediate that undergoes irreversible C–C scission from gas-phase butane and a H*-covered surface:

$$C_4H_{10}(g) + \ell H^* \rightleftharpoons C_4H_{10-y}^{\ell^*\ddagger} + \lambda H_2(g) \qquad \lambda = \frac{y+\ell}{2} \tag{7}$$

Using Eqs. (6) and (7), the hydrogenolysis turnover rate can be calculated using the free energy of Eq. (7) (the effective free energy

barrier, $\Delta G^{\ddagger}$):

$$\frac{r}{[L]} = \frac{k_B T}{h} exp\left(\frac{-\Delta G^{\ddagger}}{RT}\right) \frac{(C_4H_{10})}{(H_2)^{\lambda}} \quad (8)$$

$\Delta G^{\ddagger}$, here, is split into two contributions:

$$\Delta G^{\ddagger} = \Delta G_k + \Delta G_{des} \quad (9)$$

by splitting Eq. (7) into:

$$\ell H^* \rightleftharpoons \ell^* + \frac{\ell}{2} H_2(g) \qquad \Delta G_{des} \quad (10)$$

$$C_4H_{10}(g) + \ell^* \rightleftharpoons C_4H_{10-y}^{\ell *\ddagger} + \frac{y}{2} H_2(g) \qquad \Delta G_k \quad (11)$$

where ΔG_{des} is the free energy required to desorb H* and create ℓ vacancies (Eq. (10)), and ΔG_k is the free energy associated with forming the transition state within those vacancies (Eq. (11)).

At elevated temperatures such as hydrogenolysis conditions, the polymer substrate liquifies forming a polymer melt. Continuous C–C cleavage events of this polymer melt form liquid alkane products, decreasing the molecular weight of the melt as the reaction proceeds [91]. Modelling the evolution of the molecular weight during depolymerization requires simplifications, such as assuming all aliphatic C–C bonds have equal probabilities to cleave [30,91]. This assumption is not valid for gas-phase C–C hydrogenolysis as H_2 pressure considerably shifts the ratio of unsubstituted to substituted cleavage rates, exhibiting significant differences between branched and unbranched C–C activation [58]. Similarly, n-alkane hydrogenolysis rates at non-terminal C–C bonds in n-butane and n-decane are 3 × and 6 × larger, respectively, than terminal cleavages within those n-alkanes [2]. Hydrogenolysis selectivity between substituted and unsubstituted activation can impact product branching as activating at branch points will decrease branching in products while reducing activations at branch points will lead to more branching in products.

The branching statistics of representative polymer samples help illustrate the relevance of understanding hydrogenolysis behavior at both short- and long-chain branches in low-density polyethylene (LDPE), high-density polyethylene (HDPE), and Polypropylene (PP). An industrial LDPE has approximately 15–25 short chain branches per 1000carbon atoms with some long chain branching, while other LDPE samples can have as many as 50 branches per 1000carbon atoms [92]. Linear low-density polyethylene (LLDPE) will also typically have $\leq$ 50 branches per 1000carbon atoms, like LDPE, but for LLDPE the branches are shorter than those in LDPE. An industrial HDPE has approximately 5–7 short chain branches per 1000carbon atoms with few long chain branches [93]. The short-chain branches described here for LDPE and HDPE are typically larger than methyl groups. PP, in contrast, has 333 tertiary C atoms per 1000C atoms, as every other C along the backbone has a methyl branch, and there are typically very few long-chain branches in polypropylene, although copolymerization can lead to more extensive branching in polypropylene.

Among materials studied academically, NIST linear polyethylene Standard Reference Material (SRM 1475) is a polyethylene substrate [29] with very little branching (~1.5 tertiary carbons per 1000 carbon atoms) [94]. Another polyethylene standard used in hydrogenolysis experiments [88] has 20 ethyl side chains per thousand carbon atoms [95]. Depending on the polymer of interest, the density of both short- and long-chain branches can be significant with limited study of how larger branched alkanes activate during C–C hydrogenolysis.

Importantly, this polymer melt impacts the thermodynamics of adsorption and bond activations occurring on the catalyst surface through solvation effects [96]. As this work is focused on how gas-phase hydrogenolysis of branched alkanes can be used to infer behavior within polymer reactions, these solvation effects are absent within all reported energy barriers. While we would expect solvent effects to impact the overall rates of reaction, we do not expect solvent-transition state interactions to be sensitive to the exact composition of the isobutane transition state as the most significant effects of a polymer melt appear to be related to the size of the adsorbates and transition states [96]. Therefore, we anticipate that the absence of solvent effects in the present study would not significantly impact the predicted mechanisms described below.

While the exact nature of the adlayer is not known at all reaction conditions (particularly those which may be most relevant to polyolefin upcycling), the reaction will occur at high coverages on surfaces covered in either H* or a hydrocarbon-derived species at the high pressures of interest; the surface will never be bare. The Most Abundant Surface Intermediate (MASI) will influence activation energies (Eqs. (9)–(11) above) and kinetic behavior. For example, the λ value for ethane hydrogenolysis on a H*-covered surface is 3, while on a bare surface, its λ value would be 2, and on an ethylidyne (CH_3C^*)-covered surface, its λ value would be 0.5, and the reaction would be zero-order in ethane (rather than first-order); see Section 3 of the SI for more details. High coverage adlayers will also influence effective free energy barriers by the energies required to desorb MASI from the surface (Eq. (9) and Eq. (10) for H* MASI) to create vacancies and will influence the free energy to form the transition state within those vacancies (Eq. (11)) through co-adsorbate interactions, both through-space and through-surface.

Kinetic behavior of gas-phase hydrogenolysis can give insights into MASI identities. For example, the hydrogenolysis of alkanes exhibits kinetic behavior that demonstrates the transition from hydrocarbon-derived to H*-covered surfaces with increasing H_2:alkane ratios. This can be seen for n-alkanes [57], branched alkanes [59], and cycloalkanes [21]. This kinetic behavior indicates two main regimes: a hydrogen-lean adlayer (positive H_2 rate dependence) at low H_2 pressures and a hydrogen-rich (negative H_2 rate dependence) adlayer at high H_2 pressures. The H_2 pressure dependence, therefore, decreases until it reaches a constant value once the surfaces become saturated in H* (for n-alkanes, this constant negative H_2 pressure dependence is − 3). Larger alkanes are more likely to lead to a hydrogen-lean adlayer, and less-noble metals (such as Ru) are also more likely to lead to a hydrogen-lean adlayer. Ru adlayers during hydrogenolysis often have more positive H_2 pressure promotion (or less negative H_2 pressure inhibition) than Ir or Pt counterparts, indicating a more hydrogen-lean adlayer [9,24,39,44,45,97,98].

During polymer hydrogenolysis, it's unclear whether the surface would be dominated in H* or hydrocarbon-derived species; we suspect the latter, although the nature of the hydrocarbon-derived species that may cover surfaces during polymer hydrogenolysis is unknown. The present work, as a result, focuses on a H*-covered surface to simplify interpretation and analysis and to bring our results in-line with gas-phase alkane hydrogenolysis experiments at high H_2:alkane ratios. While this assumption will impact the total H_2-pressure dependencies suggested here, the predictions regarding branched alkane activation mechanisms (the extent and location of dehydrogenations prior to C–C cleavage) are not likely to be impacted by this assumption of a H*-covered surface, because different C–C activation transition states would be similarly impacted by the co-adsorbates present in the adlayers. In other words, the most critical features which dictate whether the rate of C–C bond activations among different isobutane-derived species relate to the inherent stability of those intermediates, and the products they form upon C–C cleavage, rather than how they interact with the surrounding adlayer.

Treating the surface as H*-covered is a reasonable first approximation, given the high H_2 pressures present during both gas-alkane and polyolefin hydrogenolysis reactions. While positive reaction orders with respect to H_2 have been observed for Ru catalysts at low H_2 pressures indicating a hydrocarbon-derived MASI, [34,39,44,45] the majority of studies at high H_2:alkane ratios show an inhibitory impact of H_2 on hydrogenolysis rates across the metals of interest [1-3,21,23,24,56-58]. As an additional simplification, here, we calculate ΔG_k on bare surfaces, thus omitting the influence of co-adsorbate interactions on ΔG_k (and

$\Delta G^{\neq}$) while including the effects of the H*-covered surface by calculating ΔG_{des} and including those energies in $\Delta G^{\neq}$, and accounting for these H* desorptions in kinetic predictions (through ℓ in Eq. (7). This simplification also requires that we estimate (rather than calculate) ℓ for isobutane activations. Based on our prior work, we estimate that one site is required for each C atom that is partially dehydrogenated in the product of C–C activation (Step 1.4), such that reactions investigated here require 2–4 sites. Put another way, we estimate that one site is required for each carbon bonded to the metal surface in the product state. Thus, we calculate ΔG_{des} energies (from a H*-covered surface) to create 2–4 vacancies to use in Eq. (9) above.

Free energies to form vacancies were calculated on H*-covered (at 1H* per surface metal atom, 1 ML) close-packed surfaces of Ru, Ir, and Pt metals. Uncorrected ΔG_{des} values are negative at 593 K on all three metals, suggesting that DFT predicts bare surfaces at 1 bar H_2 (in absence of alkane). These values remain negative even at 300 K, conditions typical of H_2 chemisorption titration experiments that are known to result in coverages near (or even slightly exceeding) 1 ML [89,99-102]. Thus, DFT either underpredicts the strength of the M–H bonds (and thus the penalties to desorb H*), the entropy of adsorbed H*, or both. The RPBE exchange correlation functional used here is reasonably accurate, but is known to underpredict binding energies [89,103-105]. Furthermore, M–H bonds in the adlayer would interact with one another through van der Waals (dispersive) interactions, absent these DFT methods. To reduce these artifacts, dispersive energies (using DFT-D3) [83] were used to improve estimations of H* adsorption enthalpy using the RPBE functional. Furthermore, uncorrected DFT values predict that H* adsorbates have an entropy of 10–15 J mol^{-1} K^{-1} across the three metals, while experimentally measured values of H* entropy on Pt nanoparticles are closer to 50–60 J mol^{-1} K^{-1} [57,89]. The significant underpredictions of entropy arise from statistical mechanics treatments, namely the harmonic oscillator approximation, that often fail for mobile adsorbates like H* [89,103,105,106]. To correct for underpredictions of H* entropy, the entropy of adsorbed H* is adjusted by a factor of 3.5 for Ru, Ir, and Pt in this work, based on the difference between DFT-estimated and experimentally observed entropies for H* on metals [89]. Varying this entropy correction factor from 3 to 4 does not have significant impacts on dominant isobutane hydrogenolysis mechanisms on Ru, Ir, or Pt; small impacts appear as changes in the effective H_2-pressure inhibition (λ) values, as shown in Table S1 of the SI.

With both entropic and enthalpic corrections of H* desorption, adjusted ΔG_{des} for H* are positive, suggesting that surfaces would be H* covered at these conditions (see Section 4 in the SI for more details), as expected from prior work [1-3,21,56-59,90]. Thus, the ΔG_{des} values used in this work for creating 2 to 4 vacancies at 593 K range from 26–65 kJ mol^{-1} for Ru, from 18–40 kJ mol^{-1} for Ir, and 8–22 kJ mol^{-1} for Pt, indicating stronger M–H bonds on Ru than on Pt, as expected.

2.2. *Extendibility of branched C–C activation transition states*

To understand how isobutane C–C hydrogenolysis mechanisms can inform PE and PP upcycling, we consider the concept of mechanistic extendibility. Extendibility provides meaningful categories to differentiate C–C activations of model compounds by determining if the mechanism can be extended to compounds with longer alkyl chains (Fig. 1). A terminal C atom is extendable in a C–C activation transition state if it has at least one H remaining; it has not undergone complete dehydrogenation. If any of the three terminal C atoms in an isobutane-derived intermediate are fully dehydrogenated, then that transition state cannot be formed during 3-ethylpentane hydrogenolysis, and that mechanism is considered 'non-extendable'. Some intermediates can be partially extendable, for example, an isobutane-derived intermediate may have one non-extendable terminal C atom and two extendable C atoms, such that the intermediate could be derived from other methyl-substituted alkanes like 3-methylpentane, but not 3-ethylpentane (see Section 7 of the SI for more details). In contrast, fully extendable mechanisms do not fully dehydrogenate any terminal methyl groups, and thus the remaining H atoms on those terminal C atoms can be replaced with alkyl chains to form an analogous transition state for a larger compound. These categories of mechanistic extendibility allow us to lay out which mechanisms can be used to predict activations of larger alkanes, and to relate studies of small model compounds to larger compounds and polyolefins.

3. Results & Discussion

3.1. *Isobutane hydrogenolysis*

Isobutane, the simplest branched alkane, has potential to inform the mechanisms of C–C hydrogenolysis at branch points in hydrocarbons, relevant for understanding the catalytic upcycling of branched polyolefins. Previous investigations of C–C hydrogenolysis were conducted on Ir catalysts as, for those investigations, C–C hydrogenolysis was an undesired side reaction during catalytic cracking and isomerization in refinery streams [1-3]. This work builds from gas-phase Ir hydrogenolysis to investigate Ru catalysts and explores more closely the role of temperature on the alkane activation mechanism, given that Ru-catalyzed hydrogenolysis occurs at a lower temperature than Ir-catalyzed reactions. Previous studies (on Ir) determined C–C activations in isobutane occur after partial dehydrogenation of the C–C bond (similar to activations in n-alkanes). However, for isobutane, other C atoms (those outside the C–C bond) also undergo dehydrogenation which further weaken the C–C bond being cleaved, and thus isobutane reactions (on Ir) occur in species that are more dehydrogenated than those of n-alkanes and in species with more surface attachments [1,58].

For consistency and convenience, we recalculated isobutane activation pathways (reported in our prior work)[1] and barriers on Ir(111) surfaces. There are 176 possible C–C bond activations of isobutane; however, we recalculated less than the total 176 activations by excluding unlikely mechanisms, based on both the free energy required to form the activation's products (see Section 6 of the SI for more details) and prior results on Ir(111). Additionally, detailed reactant and transition state structures of isobutane hydrogenolysis with marked vacancies adjacent to the isobutane-derived intermediates can be found in Section 5 of the SI.

Isobutane activation on Ir has four mechanisms with similar effective free energy barriers ($\Delta G^{\neq}$, 191–205 kJ mol^{-1}, 593 K) that involve species that have lost 3–6H atoms compared to isobutane, leading to 2.5–4 H_2 molecules evolved (λ values) prior to C–C cleavage (Fig. 2). The similar $\Delta G^{\neq}$ values among these mechanisms are in direct contrast to C–C hydrogenolysis of linear alkanes, where one mechanism has a free energy barrier far beneath all others [2,3,55,56]. Two mechanisms with low free energy barriers (191 kJ mol^{-1}, 202 kJ mol^{-1} in Fig. 2c and d, respectively) are more dehydrogenated (y values of 5 and 6) and are not extendable. These activation mechanisms (Fig. 2c–d) would not be relevant for the activation of 3-ethylpentane, but would be relevant to methyl (or ethyl) removals from 3-methylpentane. In other words, these may give insights into activations near branch points in PP or HDPE (which have some short chains), but not of long-chain branches in LDPE activations (which typically have long chains). Two other low-barrier C–C activation mechanisms (Fig. 2e–f) have no fully dehydrogenated methyl groups, and thus are fully extendable towards the branched activations of larger compounds. Examining the C_1 products of C–C activations, reactions which form CH* as the C_1 product occur with lower barriers than those producing other C_1 products (e.g., C* or CH_3*). For all 74 C–C activation mechanisms studied for isobutane, we then predict hydrogenolysis rates (593 K, 20 kPa C_4H_{10}, 10 bar H_2) using Eq. (8). The highest-rate reaction does not correspond to the lowest $\Delta G^{\neq}$, given the unequal H_2 inhibition present for these reactions and the elevated H_2 pressure examined. The extendable mechanism, shown in Fig. 2e, has the highest DFT-predicted rate at 10 bar H_2, but would result in a H_2-pressure inhibition ($\lambda = 2.5$) lower than that measured for isobutane on

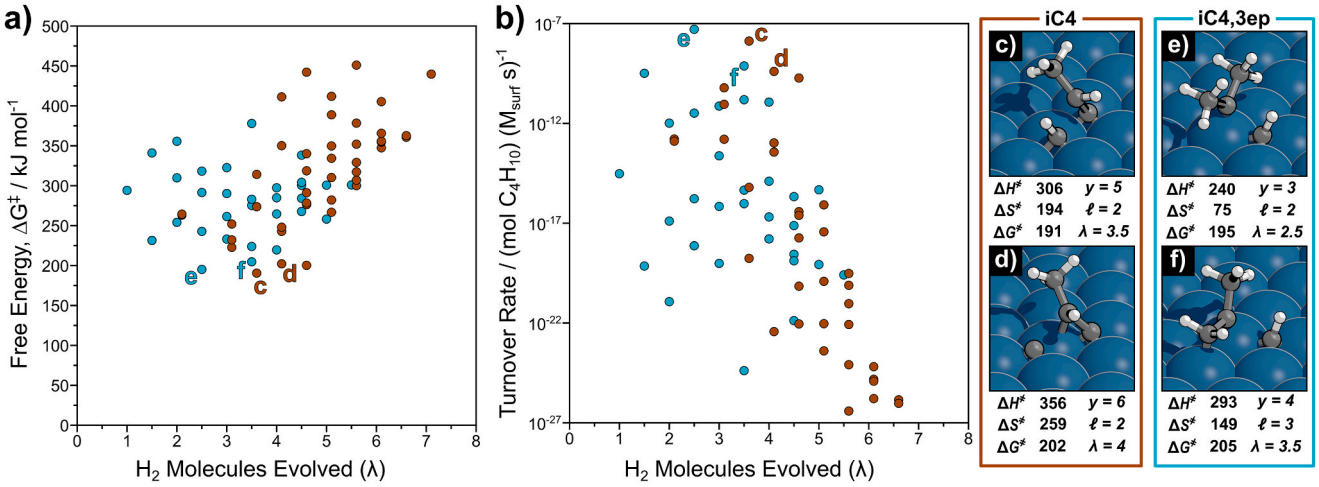

Fig. 2. (a) Free energy barriers (ΔG) for C–C bond cleavage of both extendable (light blue) and non-extendable (maroon) isobutane-derived intermediates on an Ir (111) surface (593 K, 1 bar H_2). (b) Hydrogenolysis rates for every mechanism shown in Fig. a (593 K, 20 kPa isobutane, 10 bar H_2). (c-f) Four transition state structures of the mechanisms with the highest hydrogenolysis rates in Fig. b. The enthalpy ΔH≠ (kJ mol^{-1}), entropy ΔS≠ (J mol^{-1} K^{-1}), and free energy ΔG≠ (kJ mol^{-1}) barriers are labeled below along with the H atoms removed (*y*), estimated site requirement of the transition state (ℓ), and the λ value associated with the mechanism on a H*-covered metal surface. (For interpretation of the references to color in this figure legend, the reader is referred to the web version of this article.)

Ir (λ = 4–4.5). While this extendable mechanism may be informative for 3-ethylpentane activations, experimental observations indicate that isobutane would react through a more dehydrogenated mechanism. Taking the measured kinetics and theory together, these data suggest that C–C activation is likely to occur in transition states shown in Fig. 2c or d Fig. 2c or d, involving the complete dehydrogenation of at least one vicinal methyl group, and leading to H_2-inhibitions and activation enthalpies more-similar to measured values [1,58].

For Pt, even more isobutane C–C bond activations occur with comparable ΔG≠ values. Six reactions, with ΔG≠ values ranging from 222–252 kJ mol^{-1} and 3–5H atoms removed via dehydrogenations, are shown in Fig. 3. The most reactive intermediates on Pt are similar to those found for Ir; three of the most reactive ^3C–^1C activations on Ir(111) are among the best activations on Pt(111). For Pt, four of the best mechanisms are more saturated activations (Fig. 3e–h) that are extendable to larger compounds, while the more-dehydrogenated species have slightly higher ΔG≠ values (Fig. 3c–d). The pathway with the highest DFT-predicted turnover rate (shown in Fig. 3e) is the same extendable mechanism previously predicted on Ir that did not match experimental results on Ir particles. In the case of Pt, relevant isobutane kinetic experiments have not been reported, but current DFT predictions indicate that isobutane may activate through an extendable mechanism on Pt. Overall, reactions on Pt of more-hydrogenated species occur with higher rates than on Ir, as discussed more below. In comparing ΔG≠ values between the two metals, the ΔG≠ values on Ir are ~30 kJ mol^{-1} lower than those on Pt, consistent with prior studies showing that C–C hydrogenolysis on Ir occurs with higher rates than on Pt [55,56,58]. Trends among ΔH≠ and ΔS≠ values (Figs. S1-S3 of the SI) are expected, with activation enthalpies and entropies increasing with greater dehydrogenation. Also like Ir, most (5 of 6) of the low-ΔG≠ activations on Pt involve forming a CH* species.

Ru-based catalysts are used substantially for polymer upcycling applications at lower temperatures (typically near 473 K) compared to gas phase alkane hydrogenolysis [10,29,32,34,36,39,44,107]. Three mechanisms have low ΔG≠ values (150–154 kJ mol^{-1}) on Ru(0001), and these occur after 5–7H atoms are removed by dehydrogenations (Fig. 4). All four ^3C–^1C activations with the highest hydrogenolysis rates at 10 bar H_2 (Fig. 4b) occur in species with one or more fully-dehydrogenated

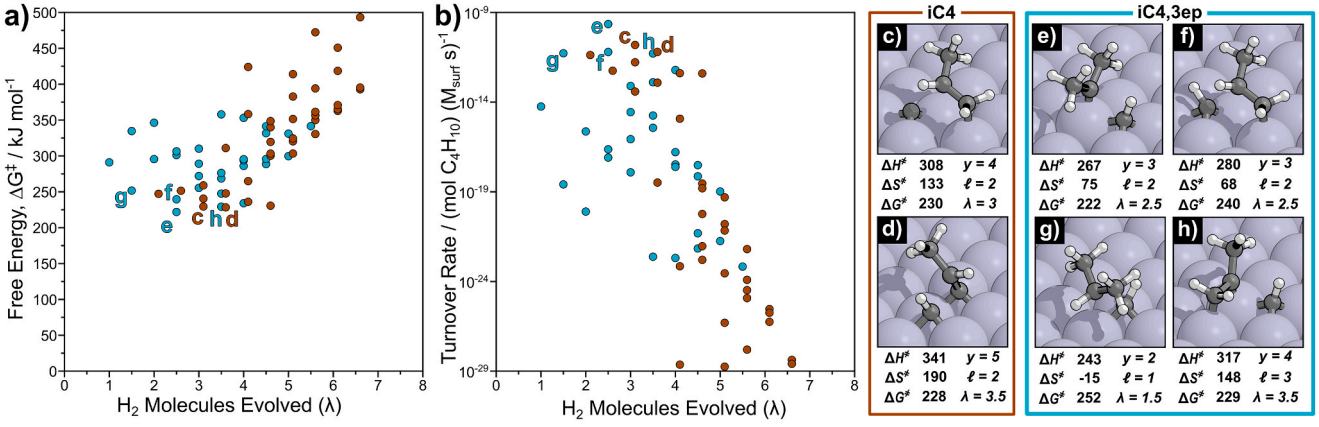

Fig. 3. (a) Free energy barriers (ΔG) for C–C bond cleavage of both extendable (light blue) and non-extendable (maroon) isobutane-derived intermediates on a Pt (111) surface (593 K, 1 bar H_2). (b) Hydrogenolysis rates for every mechanism shown in Fig. a (593 K, 20 kPa isobutane, 10 bar H_2). (c-h) Six transition state structures of the mechanisms with the highest turnover rates in Fig. b. The enthalpy ΔH≠ (kJ mol^{-1}), entropy ΔS≠ (J mol^{-1} K^{-1}), and free energy ΔG≠ (kJ mol^{-1}) barriers are labeled below along with the H atoms removed (*y*), estimated site requirement of the transition state (ℓ), and the λ value associated with the mechanism on a H*-covered metal surface and the categorical extendibility of the mechanism. (For interpretation of the references to color in this figure legend, the reader is referred to the web version of this article.)

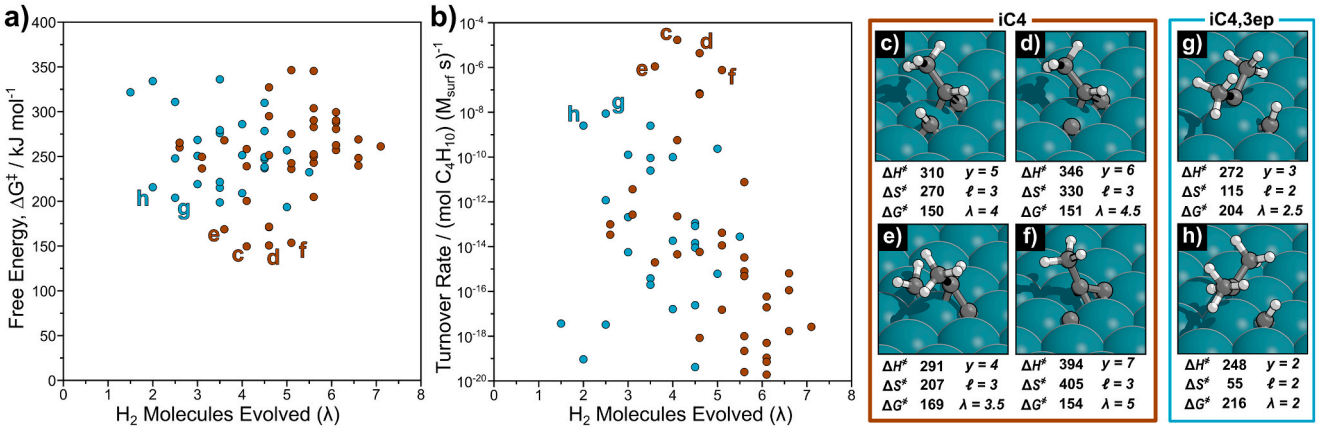

Fig. 4. (a) Free energy barriers (ΔG) for C–C bond cleavage of both extendable (light blue) and non-extendable (maroon) isobutane-derived intermediates on a Ru (0001) surface (593 K, 1 bar H_2). (b) Hydrogenolysis rates for every mechanism shown in Fig. a (593 K, 20 kPa isobutane, 10 bar H_2). (c-h) Six transition state structures of the mechanisms with the highest turnover rates in Fig. b. The enthalpy ΔH≠ (kJ mol^{-1}), entropy ΔS≠ (J mol^{-1} K^{-1}), and free energy ΔG≠ (kJ mol^{-1}) barriers are labeled below along with the H atoms removed (y), estimated site requirement of the transition state (ℓ), and the λ value associated with the mechanism on a H*-covered metal surface and the categorical extendibility of the mechanism. (For interpretation of the references to color in this figure legend, the reader is referred to the web version of this article.)

methyl groups (non-extendable mechanisms, Fig. 4c–f). This suggests that isobutane activation mechanisms on Ru would likely be different from the activations of 3-ethylpentane or long-chain branches in PE on Ru catalysts. In other words, isobutane is likely a poor model compound for gaining insights into the reactions of long-chain branch points. Two of the best mechanisms (Fig. 4d,f) require two methyl groups vicinal to the chain, suggesting that they may give insights into terminal PP activations near the ends of polymer chains (not in the middle). The mechanism shown in Fig. 4c requires only one methyl group vicinal to the tertiary carbon, and thus it can give insights into PP activations (anywhere) or activations near short-chain branches in HDPE. As said, none of the four best isobutane activations could occur in 3-ethylpentane. Barriers for Ru(0001) activation are ~40 kJ mol^{-1} lower than Ir and ~70 kJ mol^{-1} lower than Pt. Again, this is consistent with prior literature on C–C hydrogenolysis and on the popularity of Ru in academic polyolefin hydrogenolysis studies as it can perform these reactions at much lower temperatures than Ir or Pt and thus avoid thermal polymer degradation. ^{3}C–^{1}C activations on Ru(0001) occur in substantially less saturated intermediates than those for Ir and Pt.

Using the data present in Figs. 2–4, DFT-predicted turnover rates can be calculated (Eq. (8)) for each C–C hydrogenolysis mechanism and then summed over all reactive intermediates (not limited to those pictured in Figs. 2–4) to give total hydrogenolysis rates (to form propane and methane from isobutane) for each metal. As discussed above, these rates assume a catalyst surface covered with hydrogen, which is not necessarily the case during polymer hydrogenolysis. Nonetheless, these

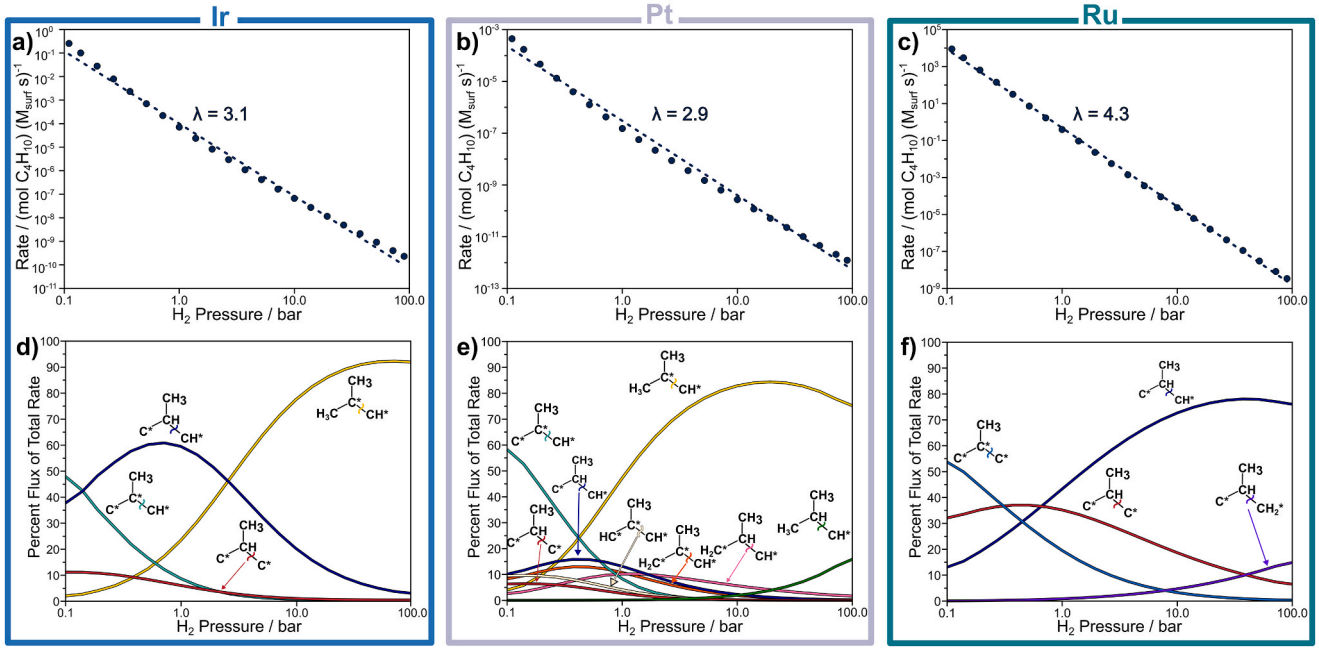

Fig. 5. Total DFT-predicted hydrogenolysis rates as a function of hydrogen pressure for C–C activation in isobutane-derived intermediates present in Figs. 2-4 on (a) Ir(111), (b) Pt(111), and (c) Ru(0001) surfaces (593 K, 20 kPa isobutane). All isobutane mechanisms are present in the rate depicted in dark blue with the hydrogenolysis rate inhibition labeled. The percent flux of the total rate for dominant mechanisms is shown for (d) Ir(111), (e) Pt(111), and (f) Ru(0001) surfaces at the same conditions. Each mechanism is labeled with an isobutane schematic with the cleavage color coded to the associated percent flux curve. (For interpretation of the references to color in this figure legend, the reader is referred to the web version of this article.)

results may give insights into reactivity trends between the three metals of interest and between isobutane and larger model branched alkanes in subsequent sections.

Estimated turnover rates, as functions of H_2 pressure, are shown in Fig. 5 at 593 K. Ru turnover rates are roughly 10^4-times higher than Ir and 10^7-times higher than Pt. Ru turnover rates are also more inhibited by H_2 pressure, with a DFT-predicted λ value (4.3) that is greater than that for Ir (λ = 3.1) or Pt (λ = 2.9). As stated earlier, the DFT-predicted λ value for isobutane is lower than that measured on Ir, suggesting that the λ values shown here may under-predict measured behavior on Ru and Pt; no such measurements exist at high H_2/alkane ratios. This also demonstrates the challenge in conveying uncertainties in these DFT-estimated values. The flux-percentages shown in Fig. 5 neglect expected uncertainties inherent to DFT calculations, such that any of the pictured mechanisms may be relevant during real reactions. For example, Fig. 2d shows an isobutane activation mechanism with a λ value of 4 that has a $\Delta G^{\neq}$ just 11 kJ mol^{-1} higher than the lowest $\Delta G^{\neq}$ predicted (Fig. 2c), which is likely within the margin of error of these DFT methods. Yet, because of the exponential dependence of rates on $\Delta G^{\neq}$ values, the mechanism depicted in Fig. 2d does not significantly contribute to the total predicted rates above 1 bar H_2 pressure in Fig. 5d. Given this, the trends predicted and displayed in Fig. 5 should be taken as qualitative, rather than quantitative. The reactivity trends (Ru > Ir > Pt) are consistent with the lower barriers shown above (Figs. 2–4), and higher rates measured for ethane hydrogenolysis at 593 K [3,55,56,58]. The changes in H_2-pressure inhibition (λ values trending as Ru > Ir > Pt) are also expected as Ru will favor the exchange of C–H bonds with C–M bonds more than Pt or Ir, as it is less noble and binds C atoms stronger than Pt or Ir. These shifts in λ values can be compared with ethane hydrogenolysis data at 593 K, as for ethane the H_2-pressure inhibition is near 3 for Ru and Ir, and lower for Pt (near 2.5), [3,55,56,58] indicating that more noble metals are less H_2-inhibited.

The slight non-linearities shown in Fig. 5a–c reflect shifts in dominant mechanisms and the degree of unsaturation in the reactive species (Fig. 5d–f). As H_2 pressure increases, the dominant mechanisms become more saturated, as expected because higher H_2 pressures lessen the entropic benefits of dehydrogenation and H_2 formation. Ir and Pt both behave similarly according to the mechanisms depicted in Figs. 2 and 3 with analogous H_2 pressure inhibitions (Fig. 5b and e). Many mechanisms contribute to the overall hydrogenolysis rate on Pt compared to Ir and Ru especially at low to medium (0.1–1 bar H_2) H_2 pressures (Fig. 5e) which is consistent with the free energy barrier comparisons (Fig. 3). Given uncertainties in $\Delta G^{\neq}$ values, this also indicates that DFT would have a hard time predicting the exact mechanism(s) for isobutane hydrogenolysis on Pt. Notably, the mechanisms that dominate at H_2 pressures above 1 bar on Pt are all extendable, suggesting that, under medium to high H_2 pressure conditions (at 593 K), isobutane may provide a reasonable surrogate for the mechanism of long-branch points present in 3-ethylpentane or polyethylene (Fig. 5e). Over the H_2 pressure range investigated, Ir activates through three non-extendable and one extendable mechanism (Fig. 5d). Given this, and the prior kinetic measurements on Ir indicating a λ value of 4–4.5 (inconsistent with the extendable mechanism), it's unlikely that reactions of isobutane on Ir occur through an extendable mechanism that would convey information about long-branch points present in 3-ethylpentane or polyethylene. Hydrogenolysis of isobutane on Ru is predicted to occur through four parallel pathways, none of which are extendable to larger branched hydrocarbons (Fig. 5f), even under high H_2 pressure conditions. This indicates that isobutane hydrogenolysis measurements would likely exhibit large λ values (≥ 4) and that the reaction mechanisms by which isobutane activates would not be reminiscent to activations of long-branch points present in 3-ethylpentane or polyethylene.

In addition to H_2-pressure effects, we also investigate the impact of temperature (400–600 K) on isobutane hydrogenolysis mechanisms at a constant H_2 pressure of 30 bar. As the temperature increases, the mechanisms of isobutane hydrogenolysis become less saturated, as expected (Fig. 6); however, the effects of temperature on the dominant mechanism are less than the H_2-pressure effects shown in Fig. 5d–f.

3.2. Predicting 3-ethylpentane hydrogenolysis from isobutane studies

Now that we have described DFT-predicted reactivity trends in isobutane hydrogenolysis mechanisms, we consider how these data can make predictions about the activation of a larger branched compound: 3-ethylpentane, to provide predictions that can be tested by future kinetic studies. There are 176 possible C–C bond activations of isobutane (all were considered, directly or by analyzing their product-formation free energies in this work). For 3-ethylpentane, considering the partial dehydrogenation of any of the 7C atoms present, the number of possible activations increases to 3040, and 24,330 for 4-propylheptane, illustrating a need to exclude activations likely to be less favorable using product formation energies. For activations of unsubstituted bonds in linear alkanes, the mechanism does not seem to change (by measured λ values or by DFT predictions) as you compare ethane and decane, and even unsubstituted bonds in branched alkanes and cycloalkanes, appear to react by the same mechanism as unsubstituted bonds in linear alkanes. The consistency of the measured λ values and DFT-predicted free energies indicates that the smallest model compound can be informative (potentially) to any unsubstituted C–C bond in basically any alkane. For branched alkanes, however, we have shown in prior work and above that reactions often occur following the complete dehydrogenation of one (or more) terminal methyl groups in isobutane, neopentane, or 2,3-dimethylbutane. Those mechanisms, therefore, cannot be replicated for compounds with larger branches, such as 3-ethylpentane, 4-propylheptane, or many of the branches present in polyethylene.

We thus filter the data to only consider extendable mechanisms (light

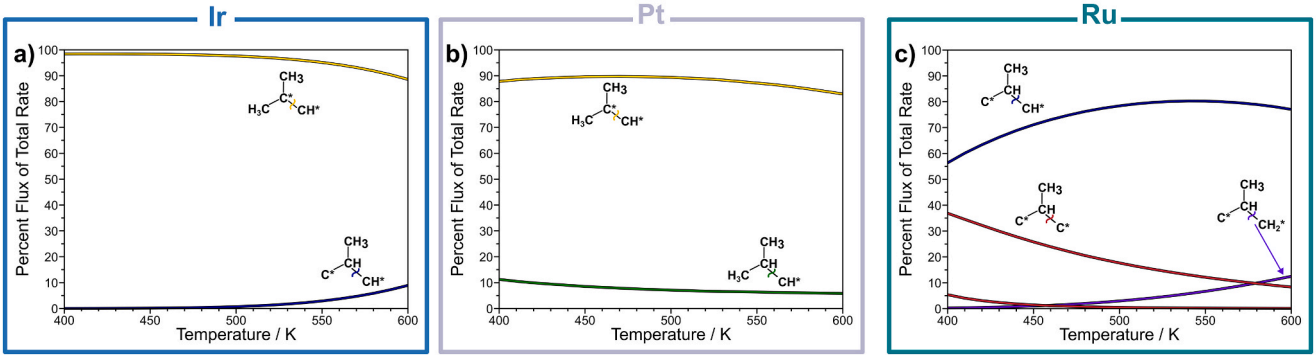

Fig. 6. Percent flux of the total rate for dominant mechanisms of isobutane hydrogenolysis on (a) Ir(111), (b) Pt(111), and (c) Ru(0001) surfaces as a function of temperature from 400 to 600 K (30 bar H_2 pressure, 20 kPa isobutane pressure). Each mechanism is labeled with an isobutane schematic with the cleavage color coded to the associated percent flux curve.

blue dots in Figs. 2-4), and we use that data to calculate turnover rates (Eq. (8)) for each mechanism and total extendable hydrogenolysis rates for each metal (Fig. 7a). The best extendable mechanisms on Ir (Fig. 7b-c) are the same as two reactive intermediates on Pt (Fig. 7d and f), and notably, one extendable mechanism dominates on every metal at these conditions (Fig. 7b, d, and g). On Ru, most of the reactive species are still more-dehydrogenated than their Ir and Pt counterparts (Fig. 7i–j), especially at higher temperatures (Fig. 7a). Also, the ethyl fragment being cleaved from 3-ethylpentane would likely be in the form of an alkylidyne (CH_3C^*), just as the C_1 cleavage fragments from isobutane are almost all CH* groups. The reactivity trends among Ir, Pt, and Ru remain similar to previously discussed trends at 593 K, with Ru turnover rates being much higher (10^2-times higher than Ir and 10^4-times higher than Pt) and more inhibited by H_2 pressure ($\lambda = 3.5$, 2.6, and 2.7 for Ru, Ir, and Pt, respectively). Based on these predictions, reactions of 3-ethylpentane would be less dehydrogenated than reactions of isobutane on any of the three metals of interest and would be less H_2-inhibited at low temperature (473 K) than at higher temperature (593 K) for Ru, while on Ir and Pt the degree of H_2-inhibition is essentially unchanged between those temperatures.

These predictions, however, enforce that the terminal methyl groups present (in yellow in Fig. 7) are, themselves, not partially dehydrogenated during 3-ethylpentane hydrogenolysis. It may be reasonable to assume that the only C atoms directly involved in the branch point activation of 3-ethylpentane are among those 4C atoms closest to the branch point, but that remains to be directly observed through kinetic measurements or direct DFT predictions. Perhaps more C atoms are involved for 3-ethylpentane, rendering the predictions in Fig. 7 to be unreliable, would 3-ethylpentane then be an appropriate model for 4-propylheptane reactions? Given a branched alkane of arbitrary size, the number of C atoms directly interacting with the surface (as opposed to those present only as alkyl chains) remains unknown, as well as how that number would depend on reaction conditions, the coverage of co-adsorbed species on the surface, and the identity of those co-adsorbates.

4. Conclusions

Hydrogenolysis of isobutane on Ir(111), Pt(111), and Ru(0001) surfaces proceeds through reactions that often involve the dehydrogenation of 3C atoms on Ru, and primarily 2C atoms on Ir and Pt prior to C–C cleavage. DFT-predicted mechanisms on Ir show many pathways with similar activation free energies ($\Delta G^{\ddagger}$), including some that have estimated λ values similar to those measured in prior work (4–4.5). However, the mechanism with the lowest $\Delta G^{\ddagger}$ value would predict rates to be inhibited by $(H_2)^3$ ($\lambda = 3$), less than the measured value at 593 K. This suggests that DFT may underpredict the degree of dehydrogenation which occurs prior to C–C activation and/or the number of H*-atoms that need to be removed from a H*-covered surface to accommodate such transition states. On Pt, the $\Delta G^{\ddagger}$ values predict that reaction rates would be lower on Pt than on Ir and that the degree of H_2-inhibition (λ) would be lower on Pt (3) than that measured on Ir (4–4.5), both predictions are consistent with ethane hydrogenolysis measurements ($\lambda =$ 2.5 for Pt and 3 for Ir). On Ru, in contrast, DFT-predicted $\Delta G^{\ddagger}$ values suggest that the reactions occur with higher rates than on Ir or Pt and in more-dehydrogenated intermediates, leading to a λ value near 4.3 (greater than those predicted for Ir or Pt).

For all three metals, multiple reaction pathways are predicted to have similar $\Delta G^{\ddagger}$ values, such that (given the uncertainties of DFT

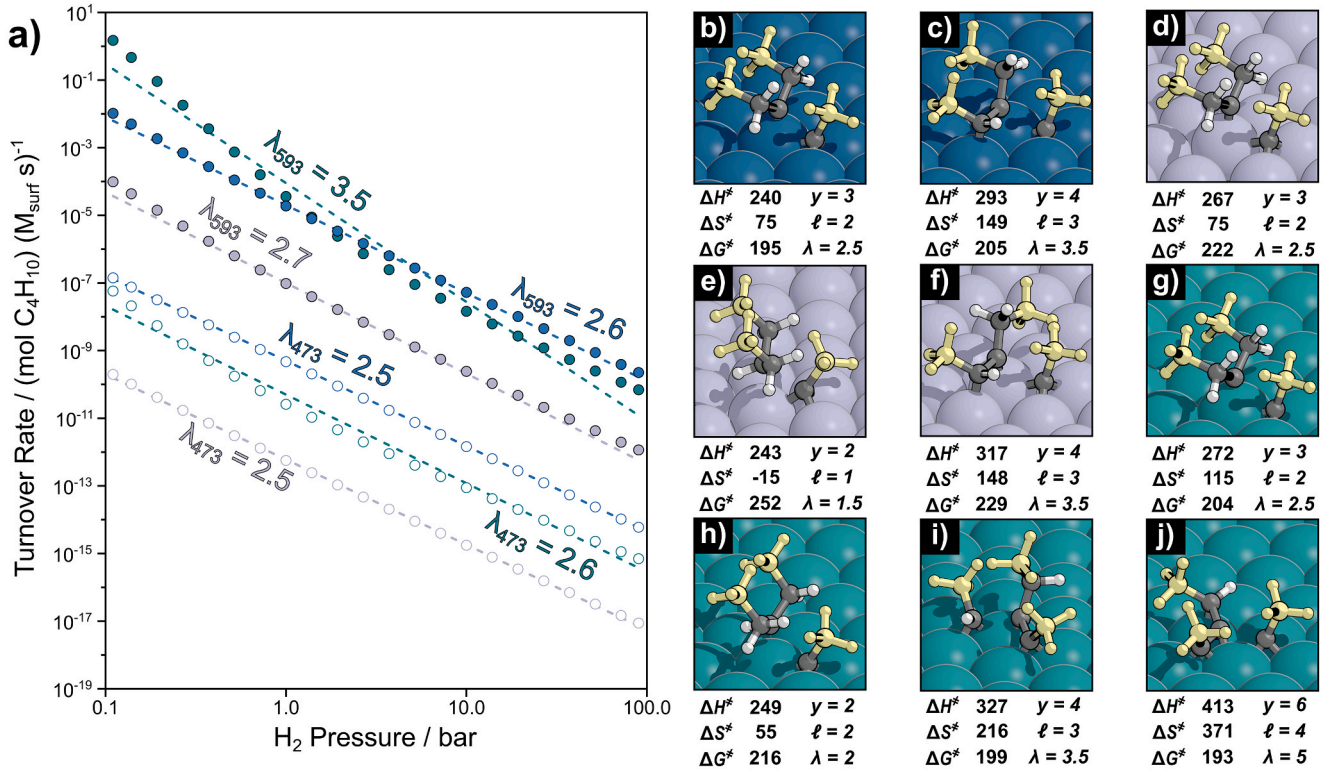

Fig. 7. (a) Total DFT-predicted hydrogenolysis rates (filled circles ●, 593 K, 20 kPa isobutane) (hollow circles ○, 473 K, 20 kPa isobutane) for C–C activation in extendable isobutane-derived intermediates present in Figs. 2-4 on Ir(111) (blue), Pt(111) (gray), and Ru(0001) (green) surfaces with associated lambda values from a power law fit colored according to metal and labelled with relevant temperature. (b-j) Transition state structures of the dominant extendable mechanisms for Ir (b-c), Pt (d-f), and Ru (g-j). The yellow methyl groups are not actually present within the transition states pictured here. The yellow groups simply represent one potential configuration of a 3-ethylpentane activation predicted by extendable isobutane activations. The enthalpy $\Delta H^{\ddagger}$ (kJ mol^{-1}), entropy $\Delta S^{\ddagger}$ (J mol^{-1} K^{-1}), and free energy $\Delta G^{\ddagger}$ (kJ mol^{-1}) barriers at 593 K are labeled below each structure along with the H atoms removed (y), estimated site requirement of the transition state (ℓ), and the λ value associated with the mechanism on a H*-covered metal surface. (For interpretation of the references to color in this figure legend, the reader is referred to the web version of this article.)

calculations) measurements would be the ultimate arbiter of which low-$\Delta G^{\neq}$ pathway is likely to occur. However, isobutane hydrogenolysis has only been reported on Ir catalysts, but not Ru or Pt, at conditions similar to the ones described here (high H_2/alkane ratios). The reactivity of these metals: Ru > Ir > Pt, is the same reactivity trend previously measured (and predicted) for ethane hydrogenolysis and can be inferred from many other alkane and polymer hydrogenolysis studies. The trend in λ values is also similar, with the more noble Pt exhibiting less H_2 inhibition (for ethane) than Ir or Ru.

Next, we considered only mechanisms which could be analogous to those present in larger compounds (e.g., 3-ethylpentane or 4-propylheptane) and thus reminiscent of those which may qualitatively describe the activation near long-chain branches in polyethylene. With that 'filter' in place, hydrogenolysis occurs in less-dehydrogenated intermediates on all three metals, with λ values predicted for 3-ethylpentane being ~0.5 lower than those for isobutane at 593 K, and ~0.8 lower at 473 K. DFT-predicted rates of isobutane hydrogenolysis reported may provide qualitative information relevant to hydrogenolysis of larger gaseous alkanes and polyolefins; however, due to assumptions made within this work, such as the surface coverage of species and the deliberate exclusion of larger alkyl extensions, quantitative predictions from this work may not be entirely appropriate. Rates of 3-ethylpentane would be expected to be higher than those for isobutane, because of the increase in dispersive interactions between the reacting alkane and the metal surface, leading to lower activation enthalpies and higher rates, consistent with rates that are proportional to alkane chain length in n-alkanes on these metals [2]. These 3-ethylpentane predictions, based on isobutane calculations, create a data set that can be tested (perhaps contradicted) with future DFT and rate measurement studies of 3-ethylpentane (or 4-propylheptane) model compounds. Furthermore, these examinations of how long-branches influence C–C hydrogenolysis mechanisms can give insights into reactions of PE and PP polymers.

CRediT authorship contribution statement

Andy Simonson: Writing – review & editing, Writing – original draft, Validation, Methodology, Investigation, Formal analysis, Data curation. **Lydia Thies:** Formal analysis, Data curation. **David Hibbitts:** Writing – review & editing, Supervision, Software, Resources, Project administration, Methodology, Investigation, Funding acquisition, Conceptualization.

Declaration of competing interest

The authors declare that they have no known competing financial interests or personal relationships that could have appeared to influence the work reported in this paper.

Acknowledgements

This work acknowledges support from the National Science Foundation Graduate Research Fellowship Program (GRFP) under Grant No. DGE-2236414. Any opinions, findings, and conclusions or recommendations expressed in this material are those of the authors and do not necessarily reflect the views of the National Science Foundation. Computational resources were provided by both the University of Florida Research Computing and the Bridges cluster at the University of Pittsburgh through allocation cts200023p from the Advanced Cyberinfrastructure Coordination Ecosystem: Services & Support (ACCESS) program.

Appendix A. Supplementary data

Supplementary data to this article can be found online at https://doi.org/10.1016/j.jcat.2025.116200.

Data availability

Data will be made available on request.

References

[1] D.D. Hibbitts, D.W. Flaherty, E. Iglesia, Role of branching on the rate and mechanism of C–C cleavage in alkanes on metal surfaces, ACS Catal. 6 (1) (2016) 469–482, https://doi.org/10.1021/acscatal.5b01950.
[2] D.D. Hibbitts, D.W. Flaherty, E. Iglesia, Effects of chain length on the mechanism and rates of metal-catalyzed hydrogenolysis of n-alkanes, J. Phys. Chem. C 120 (15) (2016) 8125–8138, https://doi.org/10.1021/acs.jpcc.6b00323.
[3] D.W. Flaherty, D.D. Hibbitts, E.I. Gürbüz, E. Iglesia, Theoretical and kinetic assessment of the mechanism of ethane hydrogenolysis on metal surfaces saturated with chemisorbed hydrogen, J. Catal. 311 (2014) 350–356, https://doi.org/10.1016/j.jcat.2013.11.026.
[4] S.S. Bello, C. Wang, M. Zhang, H. Gao, Z. Han, L. Shi, F. Su, G. Xu, A review on the reaction mechanism of hydrodesulfurization and hydrodenitrogenation in heavy oil upgrading, Energy Fuels 35 (14) (2021) 10998–11016, https://doi.org/10.1021/acs.energyfuels.1c01015.
[5] H. Wang, E. Iglesia, Thiophene hydrodesulfurization catalysis on supported Ru clusters: mechanism and site requirements for hydrogenation and desulfurization pathways, J. Catal. 273 (2) (2010) 245–256, https://doi.org/10.1016/j.jcat.2010.05.019.
[6] M. Chia, Y.J. Pagán-Torres, D. Hibbitts, Q. Tan, H.N. Pham, A.K. Datye, M. Neurock, R.J. Davis, J.A. Dumesic, Selective hydrogenolysis of polyols and cyclic ethers over bifunctional surface sites on rhodium-rhenium catalysts, J. Am. Chem. Soc. 133 (32) (2011) 12675–12689, https://doi.org/10.1021/ja2038358.
[7] D.M. Alonso, J.Q. Bond, J.A. Dumesic, Catalytic conversion of biomass to biofuels, Green Chem. 12 (9) (2010) 1493, https://doi.org/10.1039/c004654j.
[8] G. Celik, R.M. Kennedy, R.A. Hackler, M. Ferrandon, A. Tennakoon, S. Patnaik, A. M. LaPointe, S.C. Ammal, A. Heyden, F.A. Perras, M. Pruski, S.L. Scott, K. R. Poeppelmeier, A.D. Sadow, M. Delferro, Upcycling single-use polyethylene into high-quality liquid products, ACS Cent. Sci. 5 (11) (2019) 1795–1803, https://doi.org/10.1021/acscentsci.9b00722.
[9] C. Sun, J. Wang, J. Wang, M. Shakouri, B. Shi, X. Liu, Y. Guo, Y. Hu, X.-P. Wu, Y. Wang, Pt enhanced C–H bond activation for efficient and low-methane-selectivity hydrogenolysis of polyethylene over alloyed RuPt/ZrO2, Applied Catalysis b: Environment and Energy 353 (2024) 124046, https://doi.org/10.1016/j.apcatb.2024.124046.
[10] J.E. Rorrer, C. Troyano-Valls, G.T. Beckham, Y. Román-Leshkov, Hydrogenolysis of polypropylene and mixed polyolefin plastic waste over Ru/C to produce liquid alkanes, ACS Sustain. Chem. Eng. (2021), https://doi.org/10.1021/acssuschemeng.1c03786.
[11] M. Hoseini, T. Bond, Predicting the global environmental distribution of plastic polymers, Environ. Pollut. 300 (2022) 118966, https://doi.org/10.1016/j.envpol.2022.118966.
[12] A.E. Schwarz, T.N. Ligthart, E. Boukris, T. van Harmelen, Sources, transport, and accumulation of different types of plastic litter in aquatic environments: a review study, Mar. Pollut. Bull. 143 (2019) 92–100, https://doi.org/10.1016/j.marpolbul.2019.04.029.
[13] Z. Yao, H.J. Seong, Y.-S. Jang, Environmental toxicity and decomposition of polyethylene, Ecotoxicol. Environ. Saf. 242 (2022) 113933, https://doi.org/10.1016/j.ecoenv.2022.113933.
[14] K. Pabortsava, R.S. Lampitt, High concentrations of plastic hidden beneath the surface of the atlantic ocean, Nat. Commun. 11 (1) (2020) 4073, https://doi.org/10.1038/s41467-020-17932-9.
[15] A. Alsabri, F. Tahir, S.G. Al-Ghamdi, Environmental impacts of Polypropylene (PP) production and prospects of its recycling in the GCC region, Mater. Today Proc. 56 (2022) 2245–2251, https://doi.org/10.1016/j.matpr.2021.11.574.
[16] H. Shi, O.Y. Gutiérrez, G.L. Haller, D. Mei, R. Rousseau, J.A. Lercher, Structure sensitivity of hydrogenolytic cleavage of endocyclic and exocyclic C–C bonds in methylcyclohexane over supported iridium particles, J. Catal. 297 (2013) 70–78, https://doi.org/10.1016/j.jcat.2012.09.018.
[17] Z.-J. Zhao, L.V. Moskaleva, N. Rösch, Tuning the selectivity for ring-opening reactions of methylcyclopentane over Pt catalysts: a mechanistic study from first-principles calculations, J. Catal. 285 (1) (2012) 124–133, https://doi.org/10.1016/j.jcat.2011.09.021.
[18] Z.-J. Zhao, L.V. Moskaleva, N. Rösch, Ring-opening reactions of methylcyclopentane over metal catalysts, M = Pt, Rh, Ir, and Pd: a mechanistic study from first-principles calculations, ACS Catal. 3 (2) (2013) 196–205, https://doi.org/10.1021/cs3005924.
[19] Z. Wang, A. Zheng, R. Zheng, M. Li, H. Li, G. Xu, G. Xia, Selective ring opening of methylcyclopentane over surface-decorated Ir–Co bimetallic catalysts synthesized by galvanic replacement reaction, RSC Adv. 6 (107) (2016) 105063–105069, https://doi.org/10.1039/C6RA22153J.
[20] X. Dong, P. Zheng, A.-G. Zheng, H.-F. Li, G.-F. Xia, M.-F. Li, R.-Y. Zheng, B.-Q. Xu, Noble-metal efficient Pt-Ir-Co/SiO 2 catalyst for selective hydrogenolytic ring opening of methylcyclopentane, Catal. Today 316 (2018) 162–170, https://doi.org/10.1016/j.cattod.2018.03.059.
[21] D.W. Flaherty, A. Uzun, E. Iglesia, Catalytic ring opening of cycloalkanes on ir clusters: alkyl substitution effects on the structure and stability of C–C bond cleavage transition states, J. Phys. Chem. C 119 (5) (2015) 2597–2613, https://doi.org/10.1021/jp511688x.

[22] J. Weitkamp, P.A. Jacobs, J.A. Martens, Isomerization and hydrocracking of C_9 through C_{16} n-alkanes on Pt/HZSM-5 zeolite, Appl. Catal. 8 (1) (1983) 123–141, https://doi.org/10.1016/0166-9834(83)80058-X.

[23] G.C. Bond, J.C. Slaa, Catalytic and structural properties of ruthenium bimetallic catalysts: hydrogenolysis of propane and n-Butane on RuAl2O3 catalysts modified by a group 14 element, J. Mol. Catal. A: Chem 106 (1–2) (1996) 135–149, https://doi.org/10.1016/1381-1169(95)00245-6.

[24] G.C. Bond, A.D. Hooper, Modification of ruthenium catalysts for alkane hydrogenolysis, Appl. Catal. A 191 (1–2) (2000) 69–81, https://doi.org/10.1016/S0926-860X(99)00306-3.

[25] G.C. Bond, R. Yahya, B. Coq, Hydrogenolysis of alkanes. Part 5.—Effect of metal dispersion in ruthenium/alumina catalysts on the hydrogenolysis of propane and of n-butane, J. Chem. Soc., Faraday Trans. 86 (12) (1990) 2297–2301, https://doi.org/10.1039/FT9908602297.

[26] G. Bond, R. Cunningham, Alkane transformations on supported platinum catalysts, J Catal (1997).

[27] Bond, G.; Slaa, J. Catalytic and Structural Properties of Ruthenium Bimetallic Catalysts: Effects of Pretreatment on the Behaviour of Various Ru/Al,O, Catalysts in Alkane Hydrogenolysis. J Mol Catal A Chem **1995**.

[28] Bond, G. C. Metal-Catalysed Reactions of Hydrocarbons; Springer US, 2005. DOI: 10.1007/b136857.

[29] J.E. Rorrer, G.T. Beckham, Y. Román-Leshkov, Conversion of polyolefin waste to liquid alkanes with Ru-based catalysts under mild conditions, JACS Au 1 (1) (2021) 8–12, https://doi.org/10.1021/jacsau.0c00041.

[30] F. Zhang, M. Zeng, R.D. Yappert, J. Sun, Y.-H. Lee, A.M. LaPointe, B. Peters, M. M. Abu-Omar, S.L. Scott, Polyethylene upcycling to long-chain alkylaromatics by tandem hydrogenolysis/aromatization, Science 370 (6515) (2020) 437–441, https://doi.org/10.1126/science.abc5441.

[31] A. Tennakoon, X. Wu, A.L. Paterson, S. Patnaik, Y. Pei, A.M. LaPointe, S. C. Ammal, R.A. Hackler, A. Heyden, I.I. Slowing, G.W. Coates, M. Delferro, B. Peters, W. Huang, A.D. Sadow, F.A. Perras, Catalytic upcycling of high-density polyethylene via a processive mechanism, Nat. Catal. 3 (11) (2020) 893–901, https://doi.org/10.1038/s41929-020-00519-4.

[32] C. Jia, S. Xie, W. Zhang, N.N. Intan, J. Sampath, J. Pfaendtner, H. Lin, Deconstruction of high-density polyethylene into liquid hydrocarbon fuels and lubricants by hydrogenolysis over Ru catalyst, Chem Catal. 1 (2) (2021) 437–455, https://doi.org/10.1016/j.checat.2021.04.002.

[33] G. Zichittella, A.M. Ebrahim, J. Zhu, A.E. Brenner, G. Drake, G.T. Beckham, S. R. Bare, J.E. Rorrer, Y. Román-Leshkov, Hydrogenolysis of polyethylene and polypropylene into propane over cobalt-based catalysts, JACS Au 2 (10) (2022) 2259–2268, https://doi.org/10.1021/jacsau.2c00402.

[34] L. Chen, Y. Zhu, L.C. Meyer, L.V. Hale, T.T. Le, A. Karkamkar, J.A. Lercher, O. Y. Gutiérrez, J. Szanyi, Effect of reaction conditions on the hydrogenolysis of polypropylene and polyethylene into gas and liquid alkanes, React. Chem. Eng. 7 (4) (2022) 844–854, https://doi.org/10.1039/D1RE00431J.

[35] B. Du, X. Chen, Y. Ling, T. Niu, W. Guan, J. Meng, H. Hu, C.-W. Tsang, C. Liang, Hydrogenolysis-isomerization of waste polyolefin plastics to multibranched liquid alkanes, ChemSusChem 16 (3) (2023) e202202035, https://doi.org/10.1002/cssc.202202035.

[36] Y. Nakaji, M. Tamura, S. Miyaoka, S. Kumagai, M. Tanji, Y. Nakagawa, T. Yoshioka, K. Tomishige, Low-temperature catalytic upgrading of waste polyolefinic plastics into liquid fuels and waxes, Appl. Catal. B 285 (2021) 119805, https://doi.org/10.1016/j.apcatb.2020.119805.

[37] S.D. Jaydev, M.-E. Usteri, A.J. Martín, J. Pérez-Ramírez, Identifying selective catalysts in polypropylene hydrogenolysis by decoupling scission pathways, Chem Catal. (2023) 100564, https://doi.org/10.1016/j.checat.2023.100564.

[38] S. Liu, P.A. Kots, B.C. Vance, A. Danielson, D.G. Vlachos, Plastic waste to fuels by hydrocracking at mild conditions, Sci. Adv. 7 (17) (2021), https://doi.org/10.1126/sciadv.abf8283.

[39] L. Chen, L.C. Meyer, L. Kovarik, D. Meira, X.I. Pereira-Hernandez, H. Shi, K. Khivantsev, O.Y. Gutiérrez, S.J. Disordered, Sub-nanometer ru structures on CeO_2 are highly efficient and selective catalysts in polymer upcycling by hydrogenolysis, ACS Catal. (2022) 4618–4627, https://doi.org/10.1021/acscatal.2c00684.

[40] M. Chu, X. Wang, X. Wang, X. Lou, C. Zhang, M. Cao, L. Wang, Y. Li, S. Liu, T.-K. Sham, Q. Zhang, J. Chen, Site-selective polyolefin hydrogenolysis on atomic Ru for methanation suppression and liquid fuel production, Research (wash D C) 6 (2023) 0032, https://doi.org/10.34133/research.0032.

[41] H. Nguyen-Phu, T. Kwon, T. Kim, L. Thi Do, K. Hyuk Kang, I. Ro, Investigating the influence of Ru structures and supports on hydrogenolysis of polyethylene plastic waste, Chem. Eng. J. 475 (2023) 146076, https://doi.org/10.1016/j.cej.2023.146076.

[42] A. Tomer, M.M. Islam, M. Bahri, D.R. Inns, T.D. Manning, J.B. Claridge, N. D. Browning, C.R.A. Catlow, A. Roldan, A.P. Katsoulidis, M.J. Rosseinsky, Enhanced production and control of liquid alkanes in the hydrogenolysis of polypropylene over shaped Ru/CeO2 catalysts, Appl. Catal. A 666 (2023) 119431, https://doi.org/10.1016/j.apcata.2023.119431.

[43] W.-T. Lee, F.D. Bobbink, A.P. van Muyden, K.-H. Lin, C. Corminboeuf, R. R. Zamani, P.J. Dyson, Catalytic hydrocracking of synthetic polymers into grid-compatible gas streams, SSRN Journal (2020), https://doi.org/10.2139/ssrn.3696768.

[44] C. Wang, T. Xie, P.A. Kots, B.C. Vance, K. Yu, P. Kumar, J. Fu, S. Liu, G. Tsilomelekis, E.A. Stach, W. Zheng, D.G. Vlachos, Polyethylene hydrogenolysis at mild conditions over ruthenium on tungstated zirconia, JACS Au 1 (9) (2021) 1422–1434, https://doi.org/10.1021/jacsau.1c00200.

[45] C. Wang, K. Yu, B. Sheludko, T. Xie, P.A. Kots, B.C. Vance, P. Kumar, E.A. Stach, W. Zheng, D.G. Vlachos, A general strategy and a consolidated mechanism for low-methane hydrogenolysis of polyethylene over ruthenium, Appl. Catal. B 319 (2022) 121899, https://doi.org/10.1016/j.apcatb.2022.121899.

[46] L.D. Ellis, N.A. Rorrer, K.P. Sullivan, M. Otto, J.E. McGeehan, Y. Román-Leshkov, N. Wierckx, G.T. Beckham, Chemical and biological catalysis for plastics recycling and upcycling, Nat. Catal. 4 (7) (2021) 539–556, https://doi.org/10.1038/s41929-021-00648-4.

[47] H. Lv, F. Huang, F. Zhang, Upcycling waste plastics with a C-C backbone by heterogeneous catalysis, Langmuir 40 (10) (2024) 5077–5089, https://doi.org/10.1021/acs.langmuir.3c03866.

[48] M. Chu, W. Tu, S. Yang, C. Zhang, Q. Li, Q. Zhang, J. Chen, Sustainable chemical upcycling of waste polyolefins by heterogeneous catalysis, SusMat 2 (2) (2022) 161–185, https://doi.org/10.1002/sus2.55.

[49] A.H. Mason, A. Motta, A. Das, Q. Ma, M.J. Bedzyk, Y. Kratish, T.J. Marks, Rapid atom-efficient polyolefin plastics hydrogenolysis mediated by a well-defined single-site electrophilic/cationic organo-zirconium catalyst, Nat. Commun. 13 (1) (2022) 7187, https://doi.org/10.1038/s41467-022-34707-6.

[50] J.V. Lamb, Y.-H. Lee, J. Sun, C. Byron, R. Uppuluri, R.M. Kennedy, C. Meng, R. K. Behera, Y.-Y. Wang, L. Qi, A.D. Sadow, W. Huang, M.S. Ferrandon, S.L. Scott, K.R. Poeppelmeier, M.M. Abu-Omar, M. Delferro, Supported platinum nanoparticles catalyzed carbon-carbon bond cleavage of polyolefins: role of the oxide support acidity, ACS Appl. Mater. Interfaces 16 (9) (2024) 11361–11376, https://doi.org/10.1021/acsami.3c15350.

[51] J.A. Sun, P.A. Kots, Z.R. Hinton, N.S. Marinkovic, L. Ma, S.N. Ehrlich, W. Zheng, T.H. Epps, L.T.J. Korley, D.G. Vlachos, Size and structure effects of carbon-supported ruthenium nanoparticles on waste polypropylene hydrogenolysis activity, selectivity, and product microstructure, ACS Catal. (2024) 3228–3240, https://doi.org/10.1021/acscatal.3c05927.

[52] Y. Yuan, Z. Xie, K.K. Turaczy, S. Hwang, J. Zhou, J.G. Chen, Controlling product distribution of polyethylene hydrogenolysis using bimetallic Rum3 (M = Fe, Co, Ni) catalysts, Chem Bio Eng. 1 (1) (2024) 67–75, https://doi.org/10.1021/cbe.3c00007.

[53] V. Dufaud, J.-M. Basset, Catalytic hydrogenolysis at low temperature and pressure of polyethylene and polypropylene to diesels or lower alkanes by a zirconium hydride supported on silica-alumina: a step toward polyolefin degradation by the microscopic reverse of ziegler–natta polymerization, Angew. Chem. Int. Ed. (1998).

[54] X. Zhang, Y. Lu, L. Kovarik, P. Dasari, D. Nagaki, A.M. Karim, Structure sensitivity of N-butane hydrogenolysis on supported Ir catalysts, J. Catal. 394 (2021) 376–386, https://doi.org/10.1016/j.jcat.2020.10.028.

[55] A. Almithn, D. Hibbitts, Comparing rate and mechanism of ethane hydrogenolysis on transition-metal catalysts, J. Phys. Chem. C 123 (9) (2019) 5421–5432, https://doi.org/10.1021/acs.jpcc.8b11070.

[56] D.W. Flaherty, E. Iglesia, Transition-state enthalpy and entropy effects on reactivity and selectivity in hydrogenolysis of n-alkanes, J. Am. Chem. Soc. 135 (49) (2013) 18586–18599, https://doi.org/10.1021/ja4093743.

[57] A. Almithn, D. Hibbitts, Effects of catalyst model and high adsorbate coverages in ab initio studies of alkane hydrogenolysis, ACS Catal. 8 (7) (2018) 6375–6387, https://doi.org/10.1021/acscatal.8b01114.

[58] D.W. Flaherty, D.D. Hibbitts, E. Iglesia, Metal-catalyzed C-C bond cleavage in alkanes: effects of methyl substitution on transition-state structures and stability, J. Am. Chem. Soc. 136 (27) (2014) 9664–9676, https://doi.org/10.1021/ja5037429.

[59] X. Wu, A. Tennakoon, R. Yappert, M. Esveld, M.S. Ferrandon, R.A. Hackler, A. M. LaPointe, A. Heyden, M. Delferro, B. Peters, A.D. Sadow, W. Huang, Size-controlled nanoparticles embedded in a mesoporous architecture leading to efficient and selective hydrogenolysis of polyolefins, J. Am. Chem. Soc. 144 (12) (2022) 5323–5334, https://doi.org/10.1021/jacs.1c11694.

[60] E.G. Fuentes-Ordóñez, J.A. Salbidegoitia, M.P. González-Marcos, J.L. Ayastuy, M. A. Gutiérrez-Ortiz, J.R. González-Velasco, Pt/ITQ-6 zeolite as a bifunctional catalyst for hydrocracking of waste plastics containing polystyrene, J. Mater. Cycles Waste Manag. 17 (3) (2015) 465–475, https://doi.org/10.1007/s10163-014-0322-2.

[61] E.G. Fuentes-Ordóñez, J.A. Salbidegoitia, J.L. Ayastuy, M.A. Gutiérrez-Ortiz, M. P. González-Marcos, J.R. González-Velasco, High external surface pt/zeolite catalysts for improving polystyrene hydrocracking, Catal. Today 227 (2014) 163–170, https://doi.org/10.1016/j.cattod.2013.09.004.

[62] M.P. González-Marcos, E.G. Fuentes-Ordóñez, J.A. Salbidegoitia, J.R. González-Velasco, Optimization of supports in bifunctional supported Pt catalysts for polystyrene hydrocracking to liquid fuels, Top. Catal. 64 (3–4) (2021) 224–242, https://doi.org/10.1007/s11244-020-01393-x.

[63] E.G. Fuentes-Ordóñez, J.A. Salbidegoitia, M.P. González-Marcos, J.R. González-Velasco, Mechanism and kinetics in catalytic hydrocracking of polystyrene in solution, Polym. Degrad. Stab. 124 (2016) 51–59, https://doi.org/10.1016/j.polymdegradstab.2015.12.009.

[64] Z. Paál, R. Schlögl, G. Ertl, The surface state and catalytic properties of Pt black after O2-H2 cycles, Catal. Lett 12 (4) (1992) 331–344, https://doi.org/10.1007/BF00765062.

[65] I. Rodríguez-Ramos, A. Guerrero-Ruiz, Transformations of N-heptane over Pt/activated carbon catalysts, Appl. Catal. A 119 (2) (1994) 271–278, https://doi.org/10.1016/0926-860X(94)85196-4.

[66] A. Guerrero-Ruiz, B. Bachiller-Baeza, I. Rodríguez-Ramos, Catalytic properties of carbon-supported ruthenium catalysts for n-hexane conversion, Appl. Catal. A 173 (2) (1998) 231–238, https://doi.org/10.1016/S0926-860X(98)00181-1.

[67] Y. Nakagawa, S.-I. Oya, D. Kanno, Y. Nakaji, M. Tamura, K. Tomishige, Regioselectivity and reaction mechanism of Ru-catalyzed hydrogenolysis of squalane and model alkanes, ChemSusChem 10 (1) (2017) 189–198, https://doi.org/10.1002/cssc.201601204.

[68] K. Morikawa, W.S. Benedict, H.S. Taylor, The activation of specific bonds in complex molecules at catalytic surfaces. I. The carbon—hydrogen bond in methane and methane-d_4, J. Am. Chem. Soc. 58 (8) (1936) 1445–1449, https://doi.org/10.1021/ja01299a040.

[69] J.R. Engstrom, D.W. Goodman, W.H. Weinberg, Hydrogenolysis of ethane, propane, n-butane, and neopentane on the (111) and (110)-(1×2) surfaces of iridium, J. Am. Chem. Soc. 110 (25) (1988) 8305–8319, https://doi.org/10.1021/ja00233a005.

[70] H. Shi, X. Li, G.L. Haller, O.Y. Gutiérrez, J.A. Lercher, Active sites and reactive intermediates in the hydrogenolytic cleavage of C–C bonds in cyclohexane over supported iridium, J. Catal. 295 (2012) 133–145, https://doi.org/10.1016/j.jcat.2012.08.005.

[71] H. Shi, O.Y. Gutiérrez, A. Zheng, G.L. Haller, J.A. Lercher, Mechanistic pathways for methylcyclohexane hydrogenolysis over supported Ir catalysts, J. Phys. Chem. C 118 (36) (2014) 20948–20958, https://doi.org/10.1021/jp505483e.

[72] G. McVicker, M. Daage, M.S. Touvelle, C.W. Hudson, D.P. Klein, W.C. Baird Jr, B. R. Cook, J.G. Chen, S. Hantzer, D.W. Vaughan, E.S. Ellis, O.C. Freeley, Selective ring opening of naphthenic molecules, J. Catal. 210 (1) (2002) 137–148, https://doi.org/10.1006/jcat.2002.3685.

[73] G. Kresse, J. Furthmüller, Efficiency of Ab-initio total energy calculations for metals and semiconductors using a plane-wave basis set, Comp. Mater. Sci. 6 (1) (1996) 15–50, https://doi.org/10.1016/0927-0256(96)00008-0.

[74] G. Kresse, J. Hafner, Ab initio molecualr dynamics for liquid metals, Phys. Rev. B 47 (1) (1993) 558–561.

[75] G. Kresse, J. Hafner, Ab initio molecular-dynamics simulation of the liquid-metal-amorphous-semiconductor transition in germanium, Phys. Rev. B 49 (20) (1994) 14251–14269.

[76] G. Kresse, J. Furthmüller, Efficient iterative schemes for Ab initio total-energy calculations using a plane-wave basis set, PhysRevB 54 (16) (1996) 11169–11186, https://doi.org/10.1103/PhysRevB.54.11169.

[77] Kravchenko, P.; Plaisance, C.; Hibbitts, D. A New Computational Interface for Catalysis. **2019**, Published as pre-print on https://doi.org/10.26434/chemrxiv.8040737.v4. DOI: 10.26434/chemrxiv.8040737.v3.

[78] P.E. Blöchl, Projector augmented-wave method, PhysRevB 50 (24) (1994) 17953–17979, https://doi.org/10.1103/PhysRevB.50.17953.

[79] G. Kresse, D. Joubert, From ultrasoft pseudopotentials to the projector augmented-wave method, PhysRevB 59 (3) (1999) 1758–1775, https://doi.org/10.1103/PhysRevB.59.1758.

[80] B. Hammer, L.B. Hansen, J.K. Nørskov, Improved adsorption energetics within density-functional theory using revised perdew-burke-ernzerhof functionals, PhysRevB 59 (11) (1999) 7413–7421, https://doi.org/10.1103/PhysRevB.59.7413.

[81] J.P. Perdew, K. Burke, M. Ernzerhof, Generalized gradient approximation made simple, PhysRevLett.7 77 (18) (1996) 3865–3868, https://doi.org/10.1103/PhysRevLett.77.3865.

[82] Y. Zhang, W. Yang, Comment on “generalized gradient approximation made simple.”, PhysRevLett 80 (4) (1998) 890, https://doi.org/10.1103/PhysRevLett.80.890.

[83] S. Grimme, J. Antony, S. Ehrlich, H. Krieg, A consistent and accurate ab initio parametrization of Density Functional Dispersion Correction (DFT-D) for the 94 elements H-Pu, J. Chem. Phys. 132 (15) (2010) 154104, https://doi.org/10.1063/1.3382344.

[84] H.J. Monkhorst, J.D. Pack, Special Points for Brillouin-Zone Integrations, PhysRevB 13 (12) (1976) 5188–5192, https://doi.org/10.1103/PhysRevB.13.5188.

[85] J.D. Pack, H.J. Monkhorst, Special points for brillouin-zone integrations—a reply, PhysRevB 16 (4) (1977) 1748–1749, https://doi.org/10.1103/PhysRevB.16.1748.

[86] G. Henkelman, H. Jónsson, Improved tangent estimate in the nudged elastic band method for finding minimum energy paths and saddle points, J. Chem. Phys. 113 (22) (2000) 9978–9985, https://doi.org/10.1063/1.1323224.

[87] Jónsson, H.; Mills, G.; Jacobsen, K. W. Nudged Elastic Band Method for Finding Minimum Energy Paths of Transitions. In Classical and Quantum Dynamics in Condensed Phase Simulations; Berne, B. J., Ciccotti, G., Coker, D. F., Eds.; World Scientific, 1998; pp 385–404. DOI: 10.1142/9789812839664_0016.

[88] G. Henkelman, H. Jónsson, A dimer method for finding saddle points on high dimensional potential surfaces using only first derivatives, J. Chem. Phys. 111 (15) (1999) 7010–7022, https://doi.org/10.1063/1.480097.

[89] M. García-Diéguez, D.D. Hibbitts, E. Iglesia, Hydrogen chemisorption isotherms on platinum particles at catalytic temperatures: langmuir and two-dimensional gas models revisited, J. Phys. Chem. C 123 (13) (2019) 8447–8462, https://doi.org/10.1021/acs.jpcc.8b10877.

[90] A.S. Almithn, D.D. Hibbitts, Impact of metal and heteroatom identities in the hydrogenolysis of C–X bonds (X = C, N, O, S, and Cl), ACS Catal. 10 (9) (2020) 5086–5100, https://doi.org/10.1021/acscatal.0c00481.

[91] R. Yappert, B. Peters, Population balance models for polymer upcycling: signatures of the mechanism in the molecular weight evolution, J. Mater. Chem. A 10 (45) (2022) 24084–24095, https://doi.org/10.1039/D2TA04628H.

[92] Scientific Polymer Products Inc. Polyethylene, Low Density. (Catalog #: 042).

[93] Scientific Polymer Products Inc. Polyethylene, High Density. (Catalog #: 041).

[94] C.A.J. Hoeve, H.L. Wagner, P.H. Verdier, The characterization of linear polyethylene SRM 1475: I. Introduction, J Res Natl Bur Stand A Phys Chem 76A (2) (1972) 137–140, https://doi.org/10.6028/jres.076A.014.

[95] Scientific Polymer Products Inc. Polyethylene Standard (Hydrogenated Polybutadiene). (Catalog #: 1018).

[96] M. Zare, D. Sahsah, O.H. Bamidele, A. Heyden, Polyolefin melt-phase effects on alkane hydrogenolysis over Pt catalysts, Chem Catal. 4 (10) (2024) 101093, https://doi.org/10.1016/j.checat.2024.101093.

[97] G.C. Bond, J.C. Slaa, Analysis of structure-sensitivity in reactions of alkanes:N-butane hydrogenolysis on a Ru/Al2O3 catalyst, Catal. Lett 23 (3–4) (1994) 293–298, https://doi.org/10.1007/BF00811364.

[98] Galvagno, S.; Schwank, J.; Gubitosa, G.; Tauszik, G. R. Ethane and Propane Hydrogenolysis on Ru Catalysts. J. Chem. Soc., Faraday Trans. 1 **1982**, 78 (8), 2509. DOI: 10.1039/f19827802509.

[99] C.S. Brooks, Characterization of iridium catalyst surfaces by gas chemisorption, J. Colloid Interface Sci. 34 (3) (1970) 419–427, https://doi.org/10.1016/0021-9797(70)90201-8.

[100] B. Sen, M.A. Vannice, The influence of platinum crystallite size on H_2 and CO heats of adsorption and CO hydrogenation, J. Catal. 130 (1) (1991) 9–20, https://doi.org/10.1016/0021-9517(91)90087-K.

[101] B.J. Kip, F.B.M. Duivenvoorden, D.C. Koningsberger, R. Prins, Determination of metal particle size of highly dispersed rhodium, iridium and platinum catalysts by hydrogen chemisorption and EXAFS, J. Am. Chem. Soc. 108 (18) (1986) 5633–5634, https://doi.org/10.1021/ja00278a049.

[102] G. Mcvicker, R.K. Baker, R.L. Garten, E.L. Kugler, Chemisorption properties of iridium on alumina catalysts, J. Catal. 65 (1) (1980) 207–220, https://doi.org/10.1016/0021-9517(80)90295-X.

[103] A. Bajpai, P. Mehta, K. Frey, A.M. Lehmer, W.F. Schneider, Benchmark first-principles calculations of adsorbate free energies, ACS Catal. 8 (3) (2018) 1945–1954, https://doi.org/10.1021/acscatal.7b03438.

[104] J. Wellendorff, T.L. Silbaugh, D. Garcia-Pintos, J.K. Nørskov, T. Bligaard, F. Studt, C.T. Campbell, A benchmark database for adsorption bond energies to transition metal surfaces and comparison to selected DFT functionals, Surf. Sci. 640 (2015) 36–44, https://doi.org/10.1016/j.susc.2015.03.023.

[105] C.T. Campbell, J.R.V. Sellers, The entropies of adsorbed molecules, J. Am. Chem. Soc. 134 (43) (2012) 18109–18115, https://doi.org/10.1021/ja3080117.

[106] L.H. Sprowl, C.T. Campbell, L. Árnadóttir, Hindered translator and hindered rotor models for adsorbates: partition functions and entropies, J. Phys. Chem. C 120 (18) (2016) 9719–9731, https://doi.org/10.1021/acs.jpcc.5b11616.

[107] T. Xie, G.R. Wittreich, D.G. Vlachos, Multiscale modeling of hydrogenolysis of ethane and propane on Ru(0001): implications for plastics recycling, Appl. Catal. B 316 (2022) 121597, https://doi.org/10.1016/j.apcatb.2022.121597.